

# Finite element simulations of Tennessee marble under plane strain laboratory testing: Effects of sample–platen friction on shear band onset

Richard A. Albert <sup>\*,1</sup>, John W. Rudnicki

*Department of Civil Engineering, Northwestern University, 2145 Sheridan Road, Evanston, IL 60208, USA*

Received 19 April 2000

---

## Abstract

We use the finite element method to analyze a non-associated Drucker–Prager elastic–plastic material relation for Tennessee marble under plane strain laboratory test conditions. We study how the sample–platen interface boundary conditions affect the development of stress and strain in the sample and prediction for the onset of shear banding according to the Rudnicki–Rice theory. Samples that are bonded with the platen (corresponding to an infinite coefficient of friction (COF)) have all their maximum interface stresses at the outside upper corner of the test piece. When the COF is finite the stresses are not maximum in the corner but just inside of it, with the exception of the in-plane lateral normal stress, which has its maximum along the vertical centerline. Both the interface COF and the aspect ratio (the height/width ratio) affect the whole-sample axial stress–strain curves and the onset of localization. For an aspect ratio of 2.25, simulations with different COFs have whole-sample axial nominal stress versus strain curves that are coincident until late in the loading program. Then, in the vicinity of localization (near peak), these curves separate slightly from each other and the onset of localization occurs at different stress and strain values. Specifically, the stress and strain at localization onset decrease with increasing COF (from 0.01 to infinity in separate simulations) from the values for the frictionless interface. Although we focus on the 2.25 aspect ratio, our analyses with three other ratios (1.875, 1.5, and 1.0) with fixed COF show that localization onset occurs at progressively higher axial nominal stress and strain as the aspect ratio is decreased. Lastly, we find that a lower sample aspect ratio facilitates localization near the outside of the sample and close to the sample–platen interface, while the higher aspect ratio favors the onset of shear banding in the sample center. Our results demonstrate that modest variations in sample–platen friction do not significantly alter the nominal stress–strain curves but they can affect the onset and location of localization. © 2001 Elsevier Science Ltd. All rights reserved.

*Keywords:* Faulting; Localization; Shear banding; Compressive strength; Brittle failure; Dilatancy; Finite elements; Marble

---

## 1. Introduction

The problem of how to predict properly the onset of shear banding in rocks is of great importance to understanding these common features in nature. The issue relates to engineering and geophysics at micro- and macro-scales, since the

---

\* Corresponding author. Tel.: +61-2-9351-2912; fax: +61-2-9351-0184.

*E-mail address:* albert@es.usyd.edu.au (R.A. Albert).

<sup>1</sup> Present address: School of Geosciences, Division of Geology and Geophysics, University of Sydney, NSW 2006, Australia.

size of these features ranges from microcracks to km-scale geologic faults. Much work has been devoted to the issue of localization of deformation, and with respect to modeling, two main approaches, which can be considered complementary, end-member idealizations of the failure process, have emerged. One is to consider the growth, interaction, and coalescence of numerous flaws to form a zone of localized shear deformation (Horii and Nemat-Nasser, 1985; Lockner et al., 1991; Reches and Lockner, 1994). Calculations using this approach do simulate the failure process as it appears to occur in laboratory specimens. Due to the difficulty in calculating the growth and the interaction of numerous flaws, this approach is computationally intensive. Even with expected advances in computing power, calculations for complex, non-homogeneous deformation states do not seem feasible. Another drawback of this approach is that the microstructural processes in rocks are extremely complex, and the calculations require severe idealizations, usually to consider crack-like flaws in an isotropic elastic solid.

A second approach, suggested by Rudnicki and Rice (1975) and based on earlier work by Hill (1962), Mandel (1966), and Thomas (1961), is to include the details of micromechanical processes only to the extent that they contribute to macroscopically homogeneous deformation. Development of a fault, or zone of localized shear deformation, is then predicted when a bifurcation or alternative solution to homogeneous deformation becomes possible. Clearly, the predictions of this second approach depend strongly on the accuracy of the constitutive relation. Although this approach has achieved predictions that are in accord with some observations, an impediment to careful evaluation of this approach has been the difficulty of establishing accurate constitutive relations for the inelastic deformation of rock.

In this paper, we address two issues associated with the bifurcation approach to shear localization and failure. The first concerns the accuracy of determining constitutive relations from experiments. To infer constitutive relations from experiments, it is necessary to assume that the deformation in the sample is uniform. Of course, this is never exactly true but extensive experience

has indicated the appropriate geometries and end conditions to ensure that the deformation is reasonably homogeneous. Precise confirmation of this conventional wisdom by analysis has, however, been limited primarily to elasticity calculations (Peng, 1971; Al-Chalabi and Huang, 1974). In this paper we implement a non-elastic constitutive relation inferred for Tennessee marble (assuming homogeneous deformation in the test specimens) into a finite element analysis to calculate the deviations from homogeneity caused by realistic end conditions and geometries. Not surprisingly, the results confirm the conventional wisdom: for a sufficient height to width ratio and low friction at the sample–platen interface the deformation in the sample's interior is essentially homogeneous. The calculations do, however, provide insight into the detailed development of stress and strain in the sample and how deviations from homogeneity are affected by the interaction of geometry and end conditions with non-linear deformation.

The second issue we address is more subtle and concerns the effect of end conditions and geometry on the prediction of localization. The bifurcation approach assumes that deformation is homogeneous until the appearance of the shear band. In actual experiments the deformation is, of course, never perfectly homogeneous. If the localization criterion is applied pointwise in the specimen, it is possible that the condition will be met at some points well before it is met in terms of the average stress–strain behavior. If so, evaluation of the localization condition based on the average (overall) deformation in the sample may not accurately reflect the onset of failure.

## 2. Methodology

### 2.1. Tennessee marble material behavior

In this section, we briefly describe the constitutive model developed by Holcomb and Rudnicki (2000) for Tennessee marble on the basis of a suite of axisymmetric compression tests. Strain increments are decomposed into the sum of elastic and plastic portions. The elastic increments are related to the stress increments by linear isotropic elas-

ticity with shear modulus  $G$  and Poisson's ratio  $\nu$ . Inelastic behavior is assumed to occur when the stresses satisfy a yield condition of the following form:

$$\bar{\tau} = f(\sigma_m, \bar{\gamma}^p), \quad (1)$$

where  $\bar{\tau} = \sqrt{(1/2)s_{ij}s_{ij}}$  is the equivalent shear stress,  $s_{ij} = \sigma_{ij} - \sigma_m\delta_{ij}$  is the deviatoric stress, and  $\sigma_m = (1/3)\sigma_{kk}$  is the mean normal stress (positive in compression). The sole parameter used to keep track of the accumulated inelastic deformation is  $\bar{\gamma}^p$ , the equivalent plastic shear strain, defined as

$$\bar{\gamma}^p = \int_0^{e_{ij}^p} \sqrt{2 de_{ij}^p de_{ij}^p}, \quad (2)$$

where  $de_{ij}^p = d\epsilon_{ij}^p - (1/3)\delta_{ij}d\epsilon_{kk}^p$  is the deviatoric part of the inelastic increment of strain. If the stress state is on the yield surface (Eq. (1)) and the next increment of deformation causes further inelastic deformation, the stress increments must satisfy the following consistency condition in order that the stress state also be on the yield surface:

$$d\bar{\tau} = \mu(\sigma_m, \bar{\gamma}^p) d\sigma_m + h(\sigma_m, \bar{\gamma}^p) d\bar{\gamma}^p, \quad (3)$$

where  $\mu(\sigma_m, \bar{\gamma}^p) = \partial f / \partial \sigma_m$  and  $h(\sigma_m, \bar{\gamma}^p) = \partial f / \partial \bar{\gamma}^p$ . The coefficient  $\mu$  is the slope of the yield surface in the  $\bar{\tau}$  versus  $\sigma_m$  plane (for fixed  $\bar{\gamma}^p$ ) and can be given the physical interpretation as an internal friction coefficient (Fig. 1(a)). The hardening modulus  $h$  is the slope of the  $\bar{\tau}$  versus  $\bar{\gamma}^p$  at fixed  $\sigma_m$  (Fig. 1(b)). Since  $d\bar{\gamma}^p$  is necessarily non-negative, deformation increments that tend to make  $d\bar{\tau} - \mu d\sigma_m < (>) 0$  for  $h > (<) 0$  cause elastic unloading. The inelastic portion of the strain increments is given in terms of the flow potential  $\Gamma$  by

$$de_{ij}^p = d\lambda \frac{\partial \Gamma}{\partial \sigma_{ij}}, \quad (4)$$

where  $d\lambda$  is a non-negative parameter. The flow potential is assumed to have the following form:

$$\Gamma = \bar{\tau} - g(\sigma_m, \bar{\gamma}^p). \quad (5)$$

Consequently, Eq. (4) can be rewritten as

$$de_{ij}^p = d\bar{\gamma}^p \left\{ \frac{s_{ij}}{2\bar{\tau}} - \frac{1}{3}\beta\delta_{ij} \right\}, \quad (6)$$

where  $\beta(\sigma_m, \bar{\gamma}^p) = \partial g / \partial \sigma_m$  is a dilatancy factor, equal to the ratio of inelastic increments of volume strain to  $d\bar{\gamma}^p$ .

Holcomb and Rudnicki (2000) determine the functions  $f$  (and hence  $\mu$  and  $h$ ) and  $\beta$  (as shown in Fig. 1) by using a simplex method to minimize the differences between assumed forms of these functions and data from a suite of axisymmetric compression tests at confining pressures ranging from 0 to 100 MPa. We present the functions for these parameters in Appendix A. Although the elastic constants for brittle rock typically change with ongoing inelastic deformation, this change is small for Tennessee marble and consequently neglected. Therefore, the inelastic portions of the strain are determined by removing the elastic portion from the total strain based on a least squares fit for the slope of the initial loading curves.

There exists, however, a deficiency regarding the type of constitutive relation we employ in this study (i.e., a smooth yield surface with isotropic hardening) for deformation histories that have an abrupt change in the pattern of deformation. Since localization from an axisymmetric state necessarily involves such an abrupt change, predictions for localization based on this type of constitutive relation can be unrealistically conservative. Although the general form of the modification necessary to overcome this deficiency is well known (Rudnicki and Rice, 1975; Rice, 1976), the details are difficult to constrain by experiments. As this difficulty does not arise in plane strain, we focus here on calculations for that deformation state.

## 2.2. Finite element simulations

Our simulations were conducted with the commercial finite element code ABAQUS. The complex material behavior of Tennessee marble could not be accommodated by any of the standard material models in ABAQUS. Consequently, it was necessary to develop a material subroutine. For an elastically predicted stress increment (based on a specified total strain increment) which resulted in a stress state that lay outside the yield surface, we implemented a backward Euler routine (Crisfield, 1991), which is a closest-point

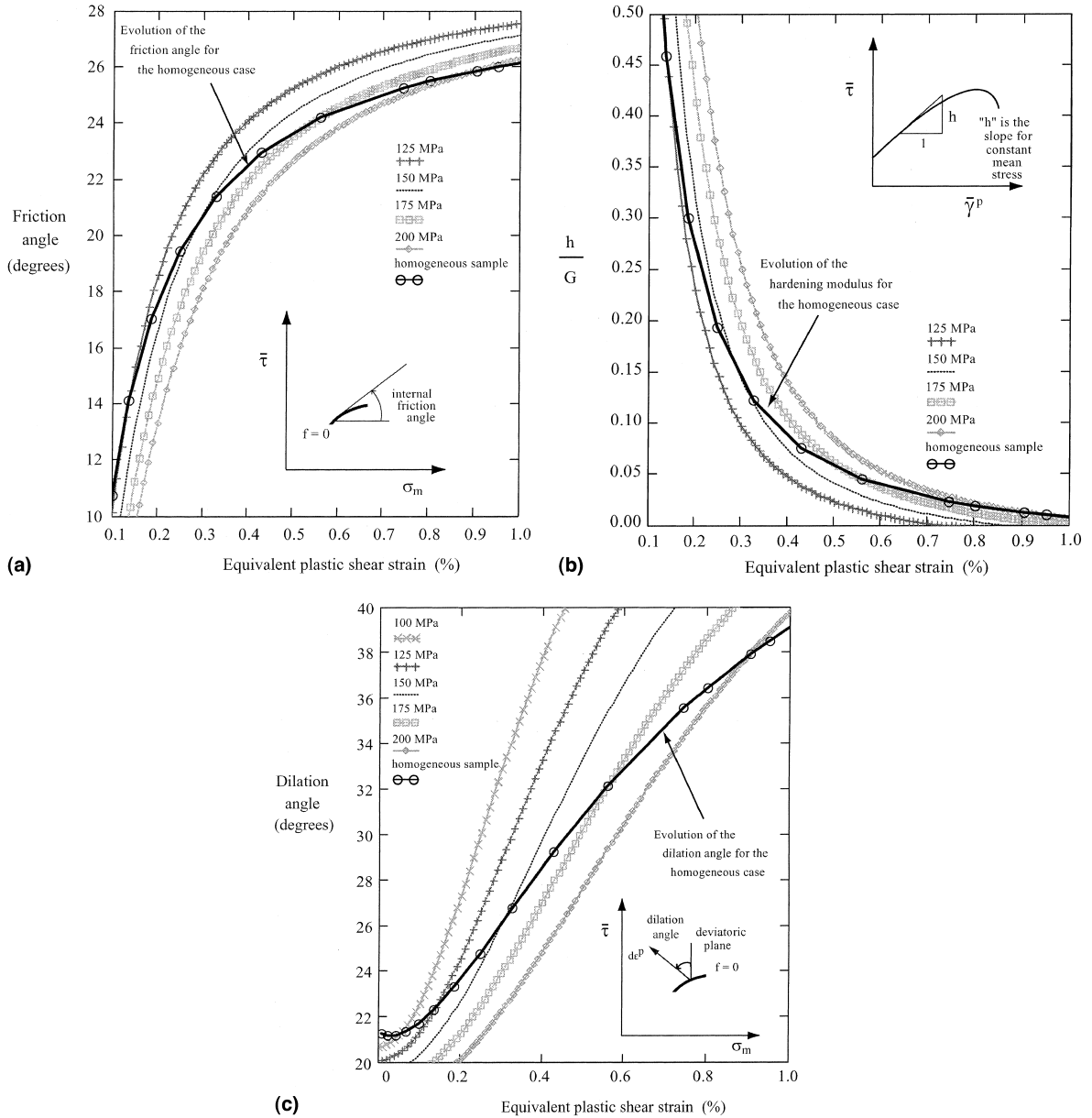


Fig. 1. In (a)–(c), we plot curves for the homogeneous sample against background curves that show the variation for fixed mean stress. The curves for plane strain deformation cut across these background curves as mean stress increases. (a) The internal friction angle ( $\tan^{-1}(\mu)$ ) in the homogeneous sample plotted versus  $\bar{\gamma}^p$  (the equivalent plastic shear strain, in %). The inset shows a graphic definition of the internal friction angle. (b) The development of the plastic hardening modulus in the homogeneous sample plotted versus  $\bar{\gamma}^p$ . The inset shows that for curves of constant mean stress the plastic hardening modulus is the slope of  $\bar{\tau}$  versus  $\bar{\gamma}^p$ . (c) The dilation angle ( $\tan^{-1}(\beta)$ ) in the homogeneous sample plotted versus  $\bar{\gamma}^p$ . The inset shows a graphic of the definition of the dilation angle.

projection method (Macari et al., 1997; Simo and Hughes, 1998) for a return to the yield surface. We verified that the stress state remained on the

yield surface at all times during plastic deformation, to ensure proper coding of the backward Euler routine.

The finite element meshes utilized three configurations that treated different amounts of friction between the marble sample and an aluminum platen. As the first configuration (homogeneous deformation) essentially treated the sample–platen interface as frictionless, we directly loaded the sample in axial compression from its initial 20 MPa hydrostatic state and there was no need to include a platen in the simulation.

In the second configuration, the sample was perfectly bonded to the platen so that there was no relative displacement between rock and metal at the interface. A quarter-sample mesh (two symmetry boundaries, one which was vertically oriented along the axial centerline and the other horizontally oriented across the sample mid-height) with 1600 elements (1344 elements in the marble test piece) is shown in Fig. 2. This condi-

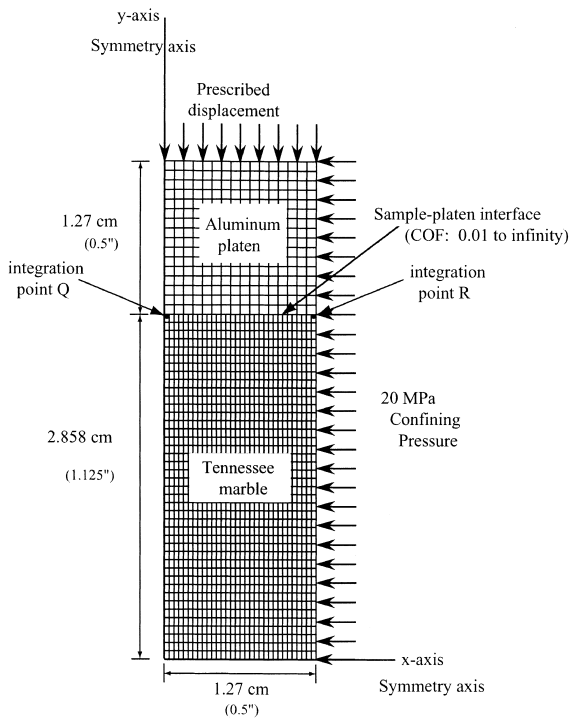


Fig. 2. A schematic of the mesh and boundary conditions used in the finite element analyses with the 2.25 aspect ratio. This mesh is used for both of the non-homogeneous configurations in our analyses. One quarter of the experimental setup is modeled, with symmetry axes along the left side and bottom boundary. There are 1600 elements in the mesh, with 1344 elements in the marble and the remainder in the metal platen.

tion at the interface allowed lateral expansion under the axial compressive load, based on Poisson's ratios of the sample and the platen. A bonded interface corresponded to an infinite COF at the interface.

The third configuration involved an interface with different finite, non-zero values of COF between the rock and the platen (0.01–0.06). For laboratory experiments, the COF of 0.02 is appropriate for a stearic acid lubricant, while 0.05 corresponds to double sheets of Teflon (Labuz and Brindell, 1993). The friction at the sample–platen interface followed a linear Coulomb friction law (Labuz and Brindell, 1993)

$$\tau_{\text{crit}} = \xi \sigma_n \quad (7)$$

In Eq. (7),  $\xi$  is the interface friction coefficient (COF),  $\sigma_n$  is the contact pressure normal to the interface, and  $\tau_{\text{crit}}$  is the critical shear stress required for slip. We implemented this boundary condition in ABAQUS via a contact analysis. In each simulation, the COF was constant throughout the entire simulation.

For the marble, we used a Poisson ratio ( $\nu$ ) of 0.30 and a shear modulus ( $G$ ) of 30 GPa. Results from detailed experimental work to determine  $G$  for Tennessee marble can be found in Olsson (1995). The marble sample had 0.0254 m (1 in) width, 0.05715 m (2.25 in) height, and unit thickness in the out-of-plane direction for a height/width aspect ratio of 2.25:1. An aluminum platen ( $\nu = 0.33$ ,  $G = 29.3$  GPa) had the same width and out-of-plane thickness as the rock sample, and height of 0.0127 m (0.5 in.). The Young's moduli for the sample and platen were nearly the same ( $E = 7.8 \times 10^{10}$ ). Corresponding to the experimental program, the sample was first loaded in hydrostatic compression to 20 MPa. Thereafter, the lateral stresses were maintained at 20 MPa while the sample was further loaded in the axial direction. The first configuration, homogeneous deformation, was perfectly hydrostatic; because of the mismatch of elastic properties, the second and third configurations (discussed below) were approximately hydrostatic, but differed from a spherical stress state at 20 MPa by less than 2%. The in-plane lateral normal stress ( $\sigma_{11}$ ) was the 20 MPa confining pressure. All analyses progressed

via displacement-control at the upper surface, and terminated when the time step fell below  $1 \mu\text{s}$ .

For each of the three configurations, all elements were four node, quadrilateral, hybrid, continuum elements. As our interest focused on the onset of localization, no special elements were needed to follow the evolution of localization beyond its onset (Borst et al., 1993).

### 3. Results

#### 3.1. Equivalent shear stress trajectories

We show typical trajectories of  $\bar{\tau}$  in  $\sigma_m$  space and  $\bar{\gamma}^p$  space for the bonded interface sample in Figs. 3 and 4, respectively. The trajectories are for three locations in the test piece: the center (lower

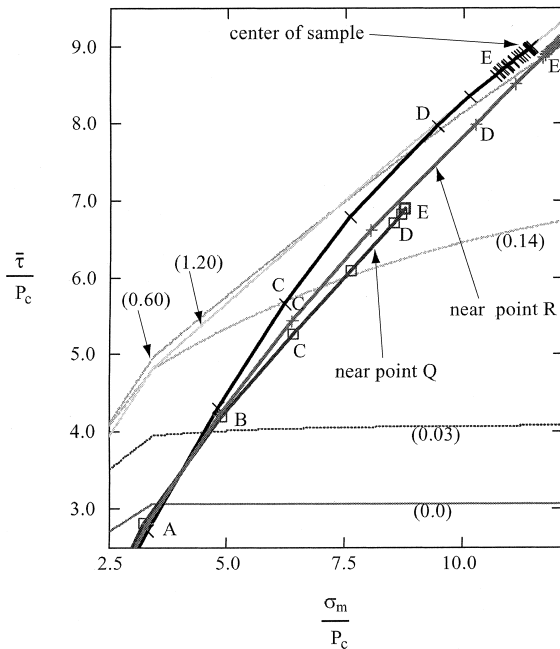


Fig. 3. The stress trajectories in  $\bar{\tau}$  versus  $\sigma_m$  space show similarities at several points in the sample for the sample with infinite interface COF. The locations maintain plastic straining once it has started, and do not exhibit softening behavior. Contours of constant equivalent plastic shear strain (with values in parentheses in %) are shown. The labels A–E pertain to specific points along the loading program for the bonded sample, and are also included in Figs. 4, 5, 6(b) and 9.

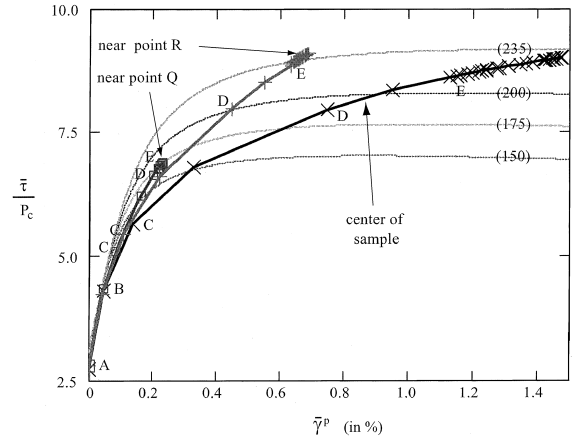


Fig. 4. The trajectories in  $\bar{\tau}$  versus  $\bar{\gamma}^p$  space show the differences in amount of plasticity by the end of simulation at different points in the sample for the case of infinite interface COF. Contours of constant mean stress (with values in parentheses in MPa) are shown. The trajectory for homogeneous deformation is largely coincident with the center of the sample curve in this figure, but shows slight softening by the end of the loading program, which is also evident in Fig. 8.

left corner of Fig. 2), and near integration points Q and R in that figure. Note that the trajectory for the homogeneous sample is essentially coincident with that of the bonded sample's center. Indeed, the whole-sample nominal stress (defined as the current axial stress divided by the undeformed cross-sectional area) versus nominal strain curves for these cases are very similar (as discussed later). Fig. 3 also shows the expansion (and contraction) of the yield surface via isotropic hardening with accumulated plastic shear strain; some contours of constant  $\bar{\gamma}^p$  are plotted with the values in parentheses. Fig. 4 shows that the amount of plastic deformation is dependent on the location in the test piece, so that the equivalent plastic shear strain is highly inhomogeneous. The labels A–E in Figs. 3 and 4 refer to specific points in the loading program, and are also shown in Figs. 5, 6 and 9.

#### 3.2. Stresses at the sample–platen interface

At the interface, the effects of different degrees of friction are most pronounced for the in-plane lateral normal stress ( $\sigma_{11}$ ) and the shear stress ( $\tau_{12}$ ). The magnitude of the out-of-plane lateral normal

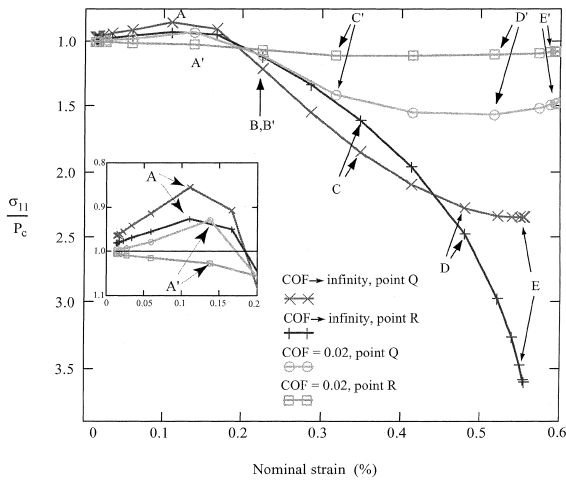


Fig. 5. The change of  $\sigma_{11}$  with whole-sample nominal strain is shown at four locations along the sample–platen interface. Two locations are in the bonded sample and two are in the 0.02 COF sample, which correspond to the locations of the integration points Q and R in Fig. 2. The simulation with the 0.02 COF shows that this stress component is significantly reduced by frictional slip along the interface compared with the bonded interface. Labels A'–E' and A–E pertain to specific points in the loading program for the 0.02 COF and the bonded sample, respectively (see Figs. 3, 4, 6(a) and (b), and 9).

stress ( $\sigma_{33}$ ) is not as strongly affected by differing COFs, presumably because this stress component is in the “zero total-strain” direction. As slip in this direction is not permitted the interface friction is unimportant. Also, the magnitude of the axial normal stress ( $\sigma_{22}$ ) is not greatly affected by different amounts of friction at the interface. (Like the contours of mean stress that are shown later in Figs. 7(a) and (b),  $\sigma_{33}$ ,  $\sigma_{22}$ , and  $\tau_{12}$  have their highest interface values in the outer corner for infinite COF and inward of this point for 0.02.) We later discuss how the interface friction’s effect on these stresses relates to the localization of the sample near the interface.

For a finite (0.02) and infinite COF models, Fig. 5 shows the  $\sigma_{11}$  variation with whole-sample nominal strain at two integration points (marked as Q and R on Fig. 2) near the sample’s upper boundary. Starting from approximately 20 MPa at the hydrostatic state, for both cases the stress component generally becomes less compressional up to the onset of plasticity (occurring after (but close to) points A and A' in the inset of Fig. 5), at

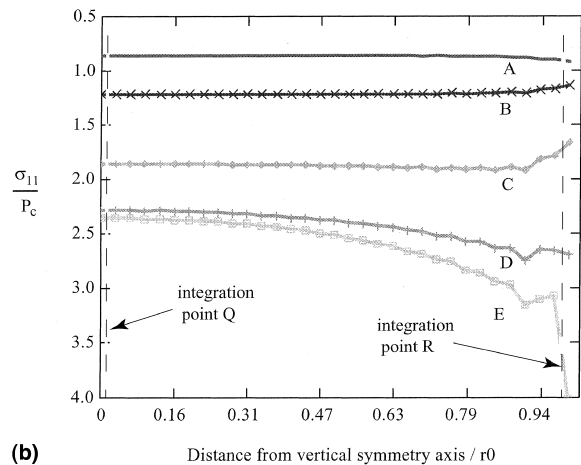
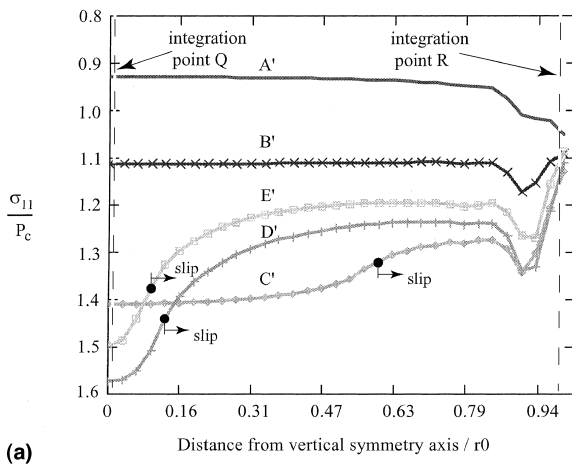


Fig. 6. The locations of integration points Q and R from Fig. 2 are shown by the dashed vertical lines, and the development of  $\sigma_{11}$  at Q and R with nominal strain is shown in Fig. 5. Regarding the  $x$ -axis,  $r0$  is the undeformed half-width of the sample (0.0127 m) from the vertical symmetry axis to the outside edge. (a) A series of plots showing how the variation of  $\sigma_{11}$  across the sample–platen interface changes for a 0.02 COF and a 2.25 aspect ratio. Curve A' is during the elastic portion of the deformation and B' is soon after plastic deformation begins. The next three curves show the extent of slip along the interface, and show the reduction of  $\sigma_{11}$  with further deformation. (b) A series of plots along the sample–platen interface that shows how  $\sigma_{11}$  evolves for a bonded interface and a 2.25 aspect ratio. The first curve is a distribution during the elastic portion of the deformation. The curves that follow are during the plastic portion of the deformation, and show the development of the maximum  $\sigma_{11}$  in the corner of the sample, in contrast with the case of 0.02 COF as shown in (a).

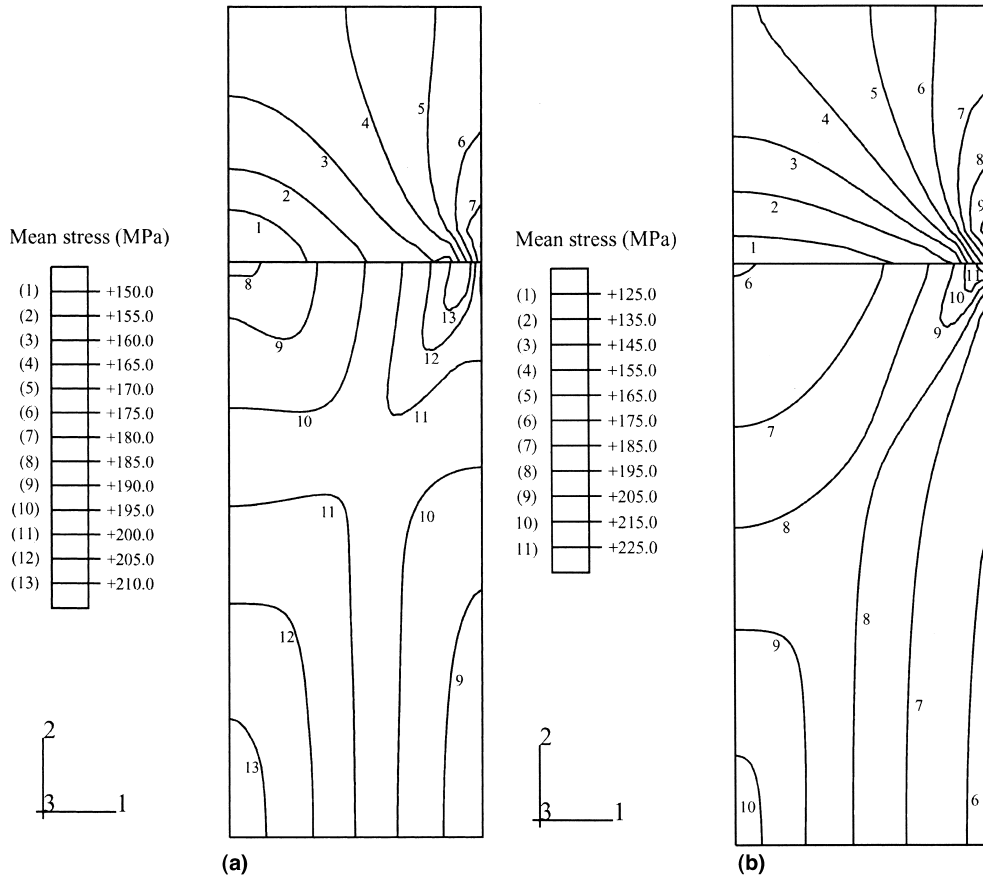


Fig. 7. (a) The distribution of pressure within the whole-sample for the 0.02 COF (and the 2.25 aspect ratio) shows the maximum pressure near the marble-metal interface but displaced to the left of the outside corner. This distribution corresponds to a deformation state soon after the first onset of localization, which occurs in the center of the sample. These contours are plotted within the undeformed coordinates of the simulation, rather than the spatial domain. (b) The distribution of pressure within the whole-sample for the bonded interface (and the 2.25 aspect ratio) shows the maximum pressure near the marble-metal interface and in the outside corner. This distribution corresponds to a deformation state soon after the onset of localization, which occurs in the center of the sample. These contours are plotted within the undeformed coordinates of the simulation, rather than the spatial domain.

which point it switches direction and becomes more compressional.

The reduction of compressional  $\sigma_{11}$  in the marble at the interface during solely elastic deformation is caused by the platen's higher Poisson ratio (0.33) relative to the marble's (0.30). Since the confining pressure is a dead load in compression, as the axial load increases (compressionally) from 20 MPa, the platen tends to laterally expand more than the sample. Due to friction at the interface, the platen pulls the sample laterally to a greater extent than the rock would expand without restraint. This results in a more tensional  $\sigma_{11}$  in the

rock at the interface, and becomes more tensional as loading progresses in the elastic regime. Considering the reduced strength of rocks in tension, it is evident how a significant mismatch in elastic properties between the sample and platen could facilitate fracture near the interface at low confining pressures, especially for a high COF. To counter this effect, in experiments the platen's elastic properties are chosen to be similar to the sample's. We later show how a high COF actually inhibits localization near the sample-platen boundary as loading progresses beyond the elastic regime.

The abrupt change in  $\sigma_{11}$  toward increasing compression occurs at the onset of plasticity in the marble while the metal remains elastic. The dilatancy that accompanies inelasticity in the rock increases the sample's "effective" Poisson ratio. The tendency of increasing lateral expansion under continued top loading causes the top-surface  $\sigma_{11}$  in the sample to become more compressional as dilatancy continues. During this period of dilatancy in the sample,  $\sigma_{11}$  in the platen near the interface becomes increasingly tensional, causing a mean stress decrease as discussed later. An important difference between the samples with the infinite versus finite-COF shows up during the interval of increasing compressional lateral stresses; the effects of frictional slip along part of the interface causes the stress buildup to taper off while the bonded sample shows further increases. Eventually  $\sigma_{11}$  starts to slightly decrease (compressionally), especially at point Q for the COF of 0.02 (D' and E' in Fig. 5). The primed and unprimed points A–E are also included in Figs. 6(a) and (b), and 9.

We follow the development of  $\sigma_{11}$  along the interface at several points in the loading program (Figs. 6(a) and (b)). In these figures, the locations of integration points Q and R from Fig. 5 are marked by the two dashed vertical lines. In Fig. 6(a) the spatial extent of frictional slip is marked, and the extent of interface slip moves from the outer edge toward the centerline with increased loading. Note that slip never occurs at the centerline because of the symmetry boundary. The lack of slip at the top centerline means  $\sigma_{11}$  remains a maximum (i.e., most compressional) there. Conversely, the simulation with the bonded interface (Fig. 6(b)) develops a maximum  $\sigma_{11}$  at the outermost point on the interface, where the tendency to expand laterally is greatest; the effective Poisson ratio of the sample rises with dilatancy but expansion is restricted by the bonding with the platen. This stress component decreases toward the centerline where it is minimum, as expected since the tendency to expand laterally is smallest at this point. We find that the location of the maximum  $\sigma_{11}$  along the interface strongly influences whether localization first occurs in the outer upper corner of the marble (for lower COF) or at the sample's center (for higher COF).

Another difference in the stress state between the two cases of non-homogeneous deformation (i.e., infinite versus finite COF) is the location of the maximum mean stress in the vicinity of the upper outer corner of the marble (Figs. 7(a) and (b)). For the bonded interface (Fig. 7(b)), the maximum mean stress (as well as all of the individual stress components) occurs in the outer corner. This stress concentration arises from the geometry of the specimen, i.e., the presence of a corner and lateral loading that is of a different magnitude than the axial load. For the interfaces with a finite, non-zero friction coefficient (0.01–0.06) (Fig. 7(a)), the maximum mean stress (as well as  $\sigma_{22}$ ,  $\sigma_{33}$ , and  $\tau_{12}$ ) occurs not in that outer corner but close to it, and toward the interior of the marble. These figures show a relatively low mean stress within the platen near the left side along the interface that increases toward the platen's outer edge. This lower mean stress (especially near the vertical symmetry axis) results because the aluminum platen's resistance to the marble's expansion causes the development of tensional  $\sigma_{11}$  (but not  $\sigma_{33}$ , which remains compressional) in the platen because of the marble's inelastic dilatancy. As one would expect, the bonded interface creates more tensional  $\sigma_{11}$  in the platen at the interface than the 0.02 COF, so that the bonded interface results in a lower mean stress in the platen near the vertical symmetry axis.

In Fig. 8 we plot the relationship between the axial nominal stress and the axial nominal strain for a homogeneously deformed sample. The departure from the elastic to plastic regimes occurs at the plus symbol. The localization onset, which occurs throughout the entire sample for homogeneous deformation, is pre-peak and marked with a blackened circle in Fig. 8. The stress–strain curves for interfaces with non-zero COFs deviate somewhat from the homogeneous case's curve, especially in the vicinity of the localization point (Fig. 9). For the fixed aspect ratio of 2.25, the stress–strain curves for all possible COFs are similar, but a closer look in the vicinity of the points of (first) localization shows some intriguing differences with respect to the stresses and strains at localization and the location of the shear banding onset within the test piece.

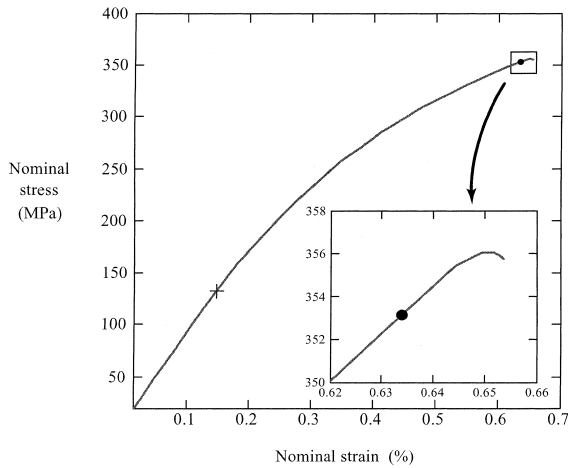


Fig. 8. The evolution of axial nominal stress and axial nominal strain for the homogeneously deformed sample shows the significant departure from linearity. The onset of plasticity is marked by the plus sign, and the onset of localization is marked by the blackened circle.

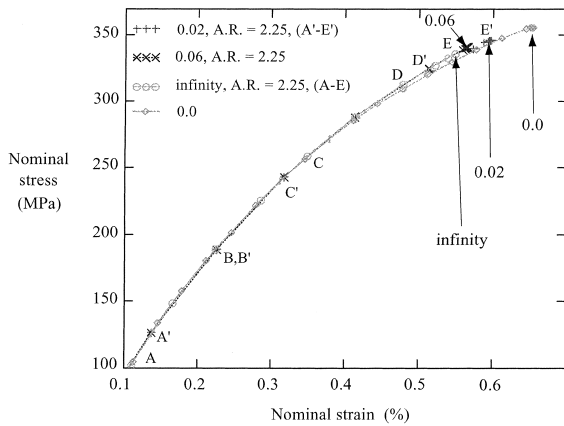


Fig. 9. Comparisons of the 2.25 aspect ratio simulations with several different COFs show that the amount of friction at the interface does not greatly alter the whole-sample axial nominal stress and strain. The differences are most pronounced at higher stress and strain. Points A–E and A'–E' correspond to points on the curves in Figs. 3–6.

3.3. Comparisons at localization

We compare the whole-sample axial nominal stresses and strains for the numerical simulations at the point in the loading program when the localization criterion of Eq. (A.1) is just reached.

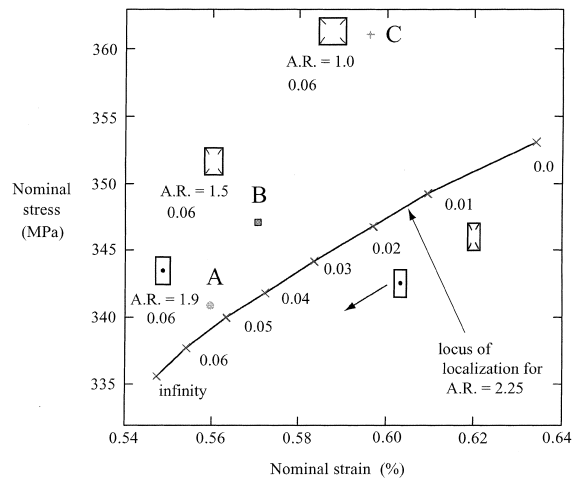


Fig. 10. The curve in this figure shows the locus of localization points for varying COF, as it depends on the whole-sample axial nominal stress and strain for the 2.25 aspect ratio. For this aspect ratio, as the interface COF is increased, the nominal stress and strain at localization decreases from that of the homogeneous case. The points marked with A, B, and C (which have no relation to points A–E in Figs. 3–6, and 9) correspond to an aspect ratio that decreases from 1.875, to 1.5, and 1.0, respectively, where each analysis has a fixed interface COF of 0.06. At point A, localization occurs in the center of the sample. At B and C, localization occurs near the upper outside corner of the marble. Our analyses show that for the 1.0 aspect ratio, the locus of localization for decreasing COF approaches the zero-COF point along the 2.25 aspect ratio locus, as expected. For the aspect ratio of 1.0, the second localization onset was prevented for the range of strains in the simulation.

The simulations show a trend toward higher sample nominal stress and nominal strain at localization onset for lower interface COF (Fig. 10). The cases with homogeneous deformation and a perfectly bonded interface are “limit” points at the highest and lowest stress/strain values, respectively, while the points of non-zero, finite COF follow the expected trend of approaching the homogeneous deformation’s localization point as the COF is reduced.

For the homogeneous case the localization criterion is met everywhere in the sample, simultaneously (by definition), and at the highest nominal stress and strain for the 2.25 aspect ratio but does not occur at the peak stress of its stress–strain curve (Fig. 8). When the COF is non-zero and finite, however, shear banding onset occurs at two different places; each “event” arises at a different

load. With a COF of 0.01, localization onset is first reached near the outer upper corner of the quarter-sample mesh (as shown in the whole-sample schematic at COF = 0.01 in Fig. 10), followed by the onset of a second localization at the center of the test piece at a slightly higher nominal stress and strain. For a COF of 0.02–0.06, localization onset always occurs first in the sample's center (shown by the whole-sample schematic near COF = 0.02 in Fig. 10), followed by a second occurrence near the outer upper corner. At the strain levels we consider, the sample with a bonded interface does not experience a second localization onset; the single onset is predicted in the center of the sample. Also, the localization locus of Fig. 10 is not parallel to any axial stress/strain trajectory for a sample with constant interface COF. Therefore, the nominal stress/strain curve for the COF of 0.02 in Fig. 9 hits the locus of Fig. 10 at a single point, approaching it from below, and passing through it toward a second localization event at slightly higher stress and strain.

For the aspect ratio of 2.25, we find that as the COF is increased, the second localization event is increasingly inhibited (Fig. 11). In this figure we plot the difference between the current (i.e., at first localization) hardening modulus and the critical hardening modulus at localization for all of the 2.25 aspect ratio simulations. For each COF, we show the difference in moduli at the occurrence of first localization but at two locations in the sample. One of the locations is the center of the sample; the second location is where the second localization will later occur for the samples with finite, non-zero COF (except for the sample with the 0.01 COF, which has its second localization at the center). That the localization criterion is met in the sample is shown by the difference in the hardening moduli being zero, either near the upper corner of the sample (for COF of 0.01) or in the center of the sample (for COFs from 0.02 to 0.06). The zero and infinite COF simulations have only a single localization event. We are not convinced that the prediction of a second localization event is physically meaningful in experiments, i.e., that it should be anticipated during a loading program. For our simulations, however, it provides a measure of the likelihood of localization at the sam-

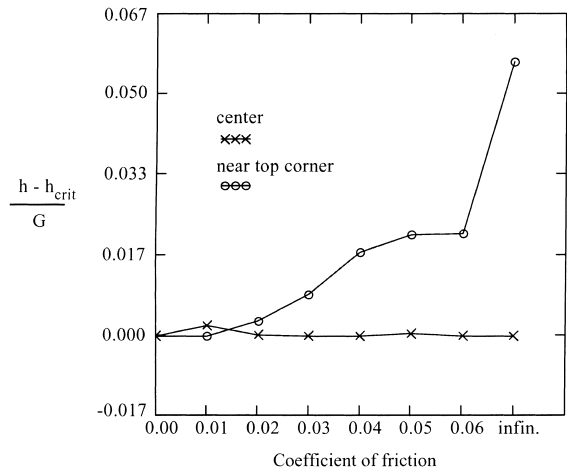


Fig. 11. This figure shows that for the 2.25 aspect ratio simulations an increase in interface COF inhibits the second onset of shear banding. The vertical axis corresponds to the difference between the current plastic hardening modulus and the critical modulus as predicted by the Rudnicki–Rice theory. The parts of the curves that do not run along the zero line correspond to the difference in moduli at the occurrence of first shear banding but at the location where the second localization is to occur at a higher deformation in the sample.

ple's center versus near the outer corner as affected by the COF.

Consideration of Fig. 11, with the trends observed in Figs. 5 and 10 explains how interface friction affects the location of shear banding onset in Tennessee marble. Fig. 5 shows that  $\sigma_{11}$  is reduced at the interface when the COF is low. Also, our analyses show that the vertical (axial) normal stress along the interface is not greatly changed when the COF is changed. Therefore, the ratio of  $\sigma_{11}$  to  $\sigma_{22}$  at the interface is reduced as the COF is reduced, which causes localization to be facilitated at the interface for low sample–platen friction. As the COF is raised, the ratio is raised, and localization near the interface is mitigated, in agreement with Fig. 11 and the whole-sample schematics for the aspect ratio of 2.25 in Fig. 10.

We also ran a series of simulations where the COF was held constant at 0.06 while the sample aspect ratio was decreased, as shown in points A, B, and C in Fig. 10. As the aspect ratio was decreased, localization was predicted at higher nominal stress and strain, and the tendency to localize was enhanced near the upper outer corner

and diminished in the sample's center. The whole-sample schematics near points A, B, and C in Fig. 10 show how the aspect ratio affects the location of shear band onset. Indeed, this result is not surprising given that at lower aspect ratio, the interface effects become increasingly important on the location of localization, favoring a site closer to the interface. This figure indicates that a change in aspect ratio from 2.25 to 1.0 has a greater affect on the nominal stress–strain curves than varying the COF at fixed aspect ratio, but the differences are still not significant.

In addition, a series of simulations with a 1.0 aspect ratio and COFs from 0.01 to infinity showed localization onset to occur exclusively near the outer corner of the sample and prevented localization in the sample's center for the range of strain in the simulations. The locus of localization for this aspect ratio (which is not shown in Fig. 10) also steadily approached the axial stress and strain of the homogeneous sample as the COF was decreased. These results support the choice of higher aspect ratio samples for experimental work (Wawersik et al., 1990; Labuz et al., 1996).

#### 4. Discussion and conclusions

Among the three configurations that cover all possible constant COFs, significant differences arise with respect to the  $\tau_{12}$  and  $\sigma_{11}$  stress components at the interface. Conversely, the magnitudes of  $\sigma_{22}$  and  $\sigma_{33}$  are not as greatly affected by the COF at the interface. For infinite COF, all stress components along the interface are highest near the outer edge, while the highest interface stresses for finite COF are slightly closer to the vertical centerline, except for  $\sigma_{11}$  which has its maximum value right at the centerline. We relate these differences to the location in the sample where the shear banding onset is predicted, discussed below. In spite of the differences, we find that the stresses and strains in the center of the sample are not significantly affected by different degrees of interface friction, and the whole-sample nominal stress versus strain curves are not greatly changed for simulations with different COFs and a fixed aspect ratio.

Interestingly, we find in another study (Albert and Rudnicki, 2000) that for axisymmetric specimens, the stresses at the center of the sample are more significantly affected by the interface COF, even for sample aspect ratios that are common in experimental work. We also find in the axisymmetric sample study a similar migration of the maximum interface mean stress,  $\sigma_{33}$ ,  $\sigma_{22}$ , etc., to the outer corner as the COF approaches infinity. Axisymmetric samples also show a more varied material response late in the loading program throughout the sample, but have not softened to the Rudnicki–Rice theory's predicted point of localization. The variety of material response includes more significant softening for all COFs (the homogeneous case is the only plane strain case that shows softening for our analyses), elastic unloading, and strain hardening (Albert and Rudnicki, 2000).

For homogeneous deformation, localization is predicted at higher axial stress and strain than for non-zero COF models with an aspect ratio of 2.25. As the amount of interface friction is increased, shear banding onset is predicted at decreasing whole-sample axial nominal stress and strain, and is increasingly favored at the sample's center while being inhibited in the vicinity of the outer upper corner.

Overall our models show well-defined trends for the onset of shear banding as the sample–platen interface friction and sample aspect ratio are varied. The results show the subtleties that arise in facilitating or inhibiting rock failure for experimentalists. The aspect of ratio of 2.25 (which matches that of the plane strain experiments on Tennessee marble (Holcomb and Rudnicki, 2000)) generally mitigates end effects and favors localization in the sample center relative to lower aspect ratios. In addition, a COF that is too low approximates the homogeneous sample's nominal stress and strain, but favors the onset of localization near the upper outer corner of the test piece. Recall that for the low COF of 0.02, for example, we found the highest compressional  $\sigma_{11}$  at the top centerline, not in the outer corner as was the case for the infinite COF. The localization near the interface for low COF occurs because the low friction causes a greater disparity between  $\sigma_{22}$  and

$\sigma_{11}$  near the outer corner, facilitating fracture. Conversely, a higher interface friction coefficient causes a larger departure from the homogeneous case's nominal stress and strain, but restricts localization to the sample's center. For high COF, the disparity between  $\sigma_{22}$  and  $\sigma_{11}$  near the interface is lessened, and localization near the interface is inhibited. Indeed, we find that the tendency to localize a second time near the outside corner is prevented (for the strain range we cover) as the interface COF approaches infinity.

### Acknowledgements

David Holcomb provided assistance in the development of the simulations according to his experiments on Tennessee marble. The ABAQUS finite element software was provided to Northwestern University under academic license from Hibbitt, Karlsson, and Sorensen, Inc. Financial support for this research was provided by the US Department of Energy, Office of Basic Energy Sciences, Geosciences Research Program through Grant number DE-FG02-93ER14344/09 to Northwestern University.

### Appendix A

For a constitutive relation with the form outlined in the main text, Rudnicki and Rice (1975) derived Eq. (A.1) for the value of the plastic hardening modulus at the start of localization. The so-called critical hardening modulus ( $h_{\text{crit}}$ ) depends on the deviatoric stress state (through the intermediate stress parameter,  $N = s_{\text{II}}/\bar{\tau}$ , where  $s_{\text{II}}$  is the intermediate deviatoric principal stress, and  $\bar{\tau}$  is an equivalent shear stress, defined in the text), and the dilation ( $\beta$ ) and friction ( $\mu$ ) factors as follows:

$$\frac{h_{\text{crit}}}{G} = \frac{(1+\nu)}{9(1-\nu)} [\beta - \mu]^2 - \frac{(1+\nu)}{2} \left( N - \frac{[\beta + \mu]}{3} \right)^2. \quad (\text{A.1})$$

The forms of the constitutive functions outlined in the text were determined by Holcomb and

Table 1  
Values of some constants

$h_0$	68.27 GPa
$h_\infty$	0.62 GPa
$\mu_0$	0.39
$\gamma_{00}$	$3.84 \times 10^{-5}$
$\gamma_{01}$	$5.26 \times 10^{-6} \text{ MPa}^{-1}$
$\sigma_0$	68.57 MPa
$\tau_0$	34.72 MPa
$\beta_0$	0.43
$\beta_\infty$	1.49
$c_0$	$2.37 \times 10^{-4}$
$c_1$	$3.71 \times 10^{-3}$
<b>B</b>	$3.32 \times 10^{-2}$

Rudnicki (2000) based on experimental work at Sandia National Laboratories. They determined the functional form of the yield surface (a Drucker–Prager surface which allows both hardening and softening), dilation factor, internal friction factor, and plastic hardening modulus. The constants in the following equations are listed in Table 1.

The specific form of the yield function in Eq. (1) that Holcomb and Rudnicki find to fit the Tennessee marble data is

$$\bar{\tau} = \tau_0 + f_1(\sigma_m, \bar{\gamma}^p) + f_2(\sigma_m), \quad (\text{A.2})$$

where

$$f_1(\sigma_m, \bar{\gamma}^p) = (h_0 + h_\infty) \gamma_0^p(\sigma_m) \tan^{-1} \left( \frac{\bar{\gamma}^p}{\gamma_0^p(\sigma_m)} \right) - h_\infty \bar{\gamma}^p \quad (\text{A.3})$$

and

$$f_2(\sigma_m) = \mu_0 \min(\sigma_m, \sigma_0). \quad (\text{A.4})$$

Forms for the friction factor  $\mu$  and the plastic hardening modulus  $h$  can be determined from  $\bar{\tau}$  by the expressions following Eq. (3) in the text.

Specifically, the internal friction factor (tangent of the internal friction angle) was

$$\mu(\sigma_m, \bar{\gamma}^p) = \mu_0 H(\sigma_0 - \sigma_m) + \frac{\gamma_{01}(h_0 + h_\infty)}{\sigma_0} \times \left\{ \tan^{-1} \left( \frac{\bar{\gamma}^p}{\gamma_0^p(\sigma_m)} \right) - \left( \frac{\bar{\gamma}^p / \gamma_0^p(\sigma_m)}{1 + [\bar{\gamma}^p / \gamma_0^p(\sigma_m)]^2} \right) \right\}, \quad (\text{A.5})$$

where  $H$  is the Heaviside step function, and the normalizing strain  $\gamma_0^p$  depends linearly on the mean stress

$$\gamma_0^p(\sigma_m) = \gamma_{00} + \gamma_{01}\sigma_m. \quad (\text{A.6})$$

As the dilation and internal friction factors are different, the plastic potential and yield function are not associated. The plastic hardening modulus has the form

$$h(\sigma_m, \bar{\gamma}^p) = \frac{h_0 + h_\infty}{1 + (\bar{\gamma}^p/\gamma_0^p(\sigma_m))} - h_\infty. \quad (\text{A.7})$$

For large values of plastic strain, this modulus tends to  $-h_\infty$ , and softening behavior.

The dilation factor is the tangent of the dilation angle (the angle that the plastic strain increment vector makes with respect to the deviatoric plane) and was determined to be

$$\beta(\sigma_m, \bar{\gamma}^p) = -B \frac{\sigma_m}{\sigma_0} + \beta_\infty - \left( \frac{\beta_\infty - \beta_0}{1 + (\bar{\gamma}^p/[c_0 - c_1(\sigma_m/\sigma_0)])^2} \right). \quad (\text{A.8})$$

## References

- Albert, R.A., Rudnicki, J.W., 2000. Non-uniformity of stress and deformation in axisymmetric finite element models of Tennessee marble. In: *Pacific Rocks 2000: Proceedings of the Fourth North American Rock Mechanics Symposium*, Seattle, WA, Balkema, pp. 999–1006.
- Al-Chalabi, M., Huang, C.L., 1974. Stress distribution within circular cylinders in compression. *Int. J. Rock Mech. Min. Sci. & Geomech. Abstr.* 11, 45–56.
- Borst, R.de., Sluys, L.J., Muhlhaus, H.-B., Pamin, J., 1993. Fundamental issues in finite element analysis of localization of deformation. *Eng. Comput.* 10, 99–121.
- Crisfield, M.A., 1991. *Non-linear Finite Element Analysis of Solids and Structures*. Vol. 1., Wiley, Chichester.
- Hill, R., 1962. Acceleration waves in solids. *J. Mech. Phys. Solids* 10, 1–16.
- Holcomb, D.J., Rudnicki, J.W., 2000. Inelastic constitutive properties and shear localization in Tennessee marble. *Mech. Cohes.-Frict. Mater.*, in press.
- Horii, H., Nemat-Nasser, S., 1985. Compression-induced microcrack growth in brittle solids; axial splitting and shear failure. *J. Geophys. Res.* 90, 3105–3125.
- Labuz, J.F., Bridell, J.M., 1993. Reducing frictional constraint in compression testing through lubrication. *Int. J. Rock Mech. Min. Sci. & Geomech. Abstr.* 30, 451–455.
- Labuz, J.F., Dai, S.-T., Papamichos, E., 1996. Plane-strain compression of rock-like materials. *Int. J. Rock Mech. Min. Sci. & Geomech. Abstr.* 33, 573–584.
- Lockner, D.A., Byerlee, J.D., Kuksenko, V., Ponomarev, A., Sidorin, A., 1991. Quasi-state fault growth and shear fracture energy in granite. *Nature* 350, 39–42.
- Macari, E.J., Weihe, S., Arduino, P., 1997. Implicit integration of elastoplastic constitutive models for frictional materials with highly non-linear hardening functions. *Mech. Cohes.-Frict. Mater.* 2, 1–29.
- Mandel, J., 1966. Conditions de stabilité et postulat de Drucker. In: Kravtchenko, J., Sirieys, P.M. (Eds.), *Rheology and Soil Mechanics*. Springer, New York, pp. 58–68.
- Olsson, W.A., 1995. Development of anisotropy in the incremental shear moduli for rock undergoing inelastic deformation. *Mech. Mater.* 21, 231–242.
- Peng, S.D., 1971. Stresses within elastic circular cylinders loaded uniaxially and triaxially. *Int. J. Rock Mech. Min. Sci. & Geomech. Abstr.* 8, 399–432.
- Reches, Z., Lockner, D.A., 1994. Nucleation and growth of faults in brittle rocks. *J. Geophys. Res.* 99, 18159–18173.
- Rice, J.R., 1976. The localization of plastic deformation. In: *Proceedings of the 14th International Congress of Theoretical and Applied Mechanics*. vol. I., North Holland, Amsterdam, pp. 207–220.
- Rudnicki, J.W., Rice, J.R., 1975. Conditions for the localization of deformation in pressure-sensitive dilatant materials. *J. Mech. Phys. Solids* 23, 371–394.
- Simo, J.C., Hughes, T.J.R., 1998. *Computational Inelasticity*. Springer, New York.
- Thomas, T.Y., 1961. *Plastic Flow and Fracture in Solids*. Academic Press, New York.
- Wawersik, W.R., Rudnicki, J.W., Olsson, W.A., Holcomb, D.J., Chau, K.T., 1990. Localization of deformation in brittle rock: theoretical and laboratory investigations. In: *Proceedings of the International Conference of Micromechanics of Failure of Quasi-brittle Materials*, Albuquerque, New Mexico, Elsevier, Amsterdam, pp. 115–124.